journal of the mechanical behavior of biomedical materials 124 (2021) 104857

Contents lists available at ScienceDirect

Journal of the Mechanical Behavior of Biomedical Materials

journal homepage: www.elsevier.com/locate/jmbbm

Research paper

Hyperelastic modeling of solid methyl cellulose hydrogel under quasi-static compression

Orel Guetta *, Daniel Rittel

Faculty of Mechanical Engineering, Technion – Israel Institute of Technology, 3200008 Haifa, Israel

ARTICLE INFO

Keywords:
Solid methylcellulose gel
Quasi-static compression
Hyperelastic modeling

ABSTRACT

Constitutive modeling of solid methyl cellulose (MC) hydrogels under quasi-static uniaxial compression is presented for a variety of compositions and test temperatures. Five constitutive models of varying complexity are examined, with the aim to identify the simplest accurate material representation. Due to the viscosity of the gel, the models were calibrated using compression tests only, with restrictions that ensure stability for other loading modes. It is found that of all the tested models, the second order polynomial constitutive model fulfills the requirements of simplicity and accuracy both for compression and predicted tension.

1. Introduction

Cellulose is one of the most common organic molecules in the world (Klemm et al., 2005). It is found as a major component in cotton fibers and in the cell walls of other plants. Its abundance lowers production costs. Cellulose is not toxic and not allergenic, hence it is bio-compatible, bio-degradable and it is FDA approved. Cellulose is widely used in many industries such as food industry, pharmaceuticals, textile and packaging (Noemi, 2011; Qiu and Hu, 2013).

Methyl cellulose (MC) is the simplest ether of cellulose and one of the most commercially used derivative of cellulose (Nasatto et al., 2015). Like cellulose, MC is colorless, nontoxic or allergenic. It is widely used as an emulsifier in the food industry and also as a prescribed laxative with millions of prescriptions in the U.S only every year (ClinCalc LLC, 2021).

MC hydrogels also have a unique property of thermally reversible solidification when heated (Schupper and Shnerb, 2005). Below its gelation temperature, the solution is in its transparent liquid phase. When heated, the solution turns into a milky white solid phase. This phase transition is an endothermic process which requires supply of energy as heat. This unique property, along with MC bio-compatibility, makes this hydrogel suitable for a variety of applications in the bio-engineering field. Drug delivery methods, 3D bio-printing , smart cell culture and soft tissue and bones reconstruction. A thorough review of the biomedical applications of MC hydrogels, as well as the fabrication techniques, can be found in the extensive reviews of Bonetti et al. (2020), Stalling et al. (2009), Altomare et al. (2016), Law et al. (2018) Kim et al. (2018).

Previous research has shown that MC gel can also solidify when the energy is supplied not only as heat but also as a mechanical impact (Parvari et al., 2018). Upon solidification, the gel absorbs some of the mechanical impact energy and uses it for the phase transition process (Senol et al., 2020). The endothermic solidification under impact makes MC a potential material for impact mitigation in order to protect bodily organs from long term damages resulting from the propagation of the shock waves through the body (Alley et al., 2011).

While the shock attenuation properties of the gel have been and still are thoroughly investigated (Rotbaum et al., 2019; Guetta et al., 2020), the extreme opposite, namely the quasi-static mechanical response of MC gels did not receive a comparable attention so far despite its importance. The applications mentioned above use methyl cellulose hydrogels as a temporary structural material, which carries loads i.e. 3D bio-printed tissue's or bone's weight (Contessi Negrini et al., 2018; Polamaplly et al., 2019; Biswas et al., 2018). For those purposes, and in order to achieve the geometrical precision of the printed product, it is crucial to model the mechanical behavior of MC hydrogels and predict their deformations under static loads.

Rotbaum et al. (2017) characterized the static and dynamic stress–strain curves of different types of solid MC hydrogels with different concentrations at different temperatures, using static compression testing and a split Hopkinson apparatus, respectively. In those experiments, 3 different types of MC gel with different level of methylation, i.e. A7C, A15C and MVM methyl cellulose hydrogels were tested. Specimens of the gels for 3 different concentrations, i.e. 2.8, 4.4 and 5.6%Wt were compressed statically at 3 different temperatures, 65, 80 and 100 °C. The experimental stress–strain curves of all the specimens had a similar shape with an upward concavity showing strain hardening.

* Corresponding author.
E-mail address: orel-gueta@campus.technion.ac.il (O. Guetta).

https://doi.org/10.1016/j.jmbbm.2021.104857
Received 25 May 2021; Received in revised form 27 July 2021; Accepted 20 September 2021
Available online 27 September 2021

List of symbols

MC	methyl cellulose
X_i	position in reference configuration
x_i	position in current configuration
$\mathbf{F}$	deformation gradient
$\mathbf{B}$	left Cauchy–Green tensor
I_i	invariants of $\mathbf{B}$
ε_{ijk}	Levi-Civita operator
$\boldsymbol{\sigma}$	Cauchy stress tensor
$W(\mathbf{B})$	strain energy density function
J	$\det(\mathbf{F})$
λ_i	principal stretches
(R, Φ, Z)	position in cylindrical coordinates in the reference configuration
(r, ϕ, z)	position in cylindrical coordinates in the current configuration
Λ	axial stretch
λ	radial stretch
C_{ij}	polynomial models' material's constants
σ_{zz}	axial stress
K, n	strain hardening model's material's constants
ε_{zz}	axial strain

This non-linear stress–strain relation of hydrogels is referred to as shear thickening (McAllister et al., 2015).

Continuum mechanics is a field which describes the mechanical behavior of materials under the assumption of continuum (Truesdell et al., 2004). One of the most commonly used continuum family of models is the hyperelastic one. Those models are often used to describe the mechanical behavior of soft materials (Volokh, 2016). A strain energy density function is assumed, whose stresses are derived from. The different models differ by their strain energy density function. A more sophisticated model will contain more material constants and will therefore better describe the mechanical behavior of the material under different loading conditions, but it will also be more difficult to calibrate. When modeling the mechanical response of a material, the desired goal is the combination of the simplest model that best describes the mechanical behavior of the tested material.

In this paper, we model the uniaxial quasi-static compression of MC gels of various compositions and test temperatures in order to facilitate future applications of this bio-material in quasi-static loading configurations. Firstly, the compressibility of the gel is determined experimentally. Next, 4 continuum based and a strain hardening constitutive models are fitted to the reported experimental stress–stretch curves characteristics (Rotbaum et al., 2017), in order to verify their respective merits. As a further verification, we model the gel's response under uniaxial tension that cannot be measured experimentally in a straightforward manner. The model predictions are compared qualitatively with published data about other gels for each investigated model.

2. Theoretical background

2.1. Hyperelasticity

The mathematical development of the constitutive stress–stretch equations for the case of a cylinder under axial compression is given in Appendix A. A brief summary of the models used in this work is detailed here.

Consider a deformation which described by the deformation gradient F_{ij}. Left Cauchy–Green tensor is defined as $\mathbf{B} = \mathbf{F}\mathbf{F}^{\mathbf{T}}$. For a certain hyperelastic strain energy density function $W(\mathbf{B})$, the stress tensor can be derived from $W(\mathbf{B})$ according to the following equation:

$$\boldsymbol{\sigma} = \frac{2}{J}\left[\left(\frac{\partial W}{\partial I_1} + I_1\frac{\partial W}{\partial I_2}\right)\mathbf{B} - \frac{\partial W}{\partial I_2}\mathbf{B}^2 + I_3\frac{\partial W}{\partial I_3}\mathbf{1}\right] \tag{1}$$

Where I_i are the invariants of $\mathbf{B}$ which are defined as:

$$\begin{aligned} I_1 &= \mathrm{trace}(\mathbf{B}) \\ I_2 &= \frac{1}{2}\left[(\mathrm{trace}(\mathbf{B})^2 - \mathrm{trace}(\mathbf{B}^2)\right] \\ I_3 &= \det(\mathbf{B}) \end{aligned} \tag{2}$$

Eq. (1) describes the relation between the strain energy density function W and the stress tensor $\boldsymbol{\sigma}$. One can use many different energy functions, depending on the selected hyperelastic model.

Alternatively, one can define the strain energy function as a function of the principal stretches λ_i, which are the eigenvalues of $\mathbf{F}$:

$$W(\mathbf{B}) = W(\lambda_1, \lambda_2, \lambda_3) \tag{3}$$

By using the spectral decomposition of $\mathbf{B}$, one can find immediately the stress tensor in its spectral form:

$$\sigma_i = \frac{\lambda_i}{\lambda_1\lambda_2\lambda_3}\frac{\partial W}{\partial \lambda_i} \qquad \text{(no sum)} \tag{4}$$

One can switch between those two approaches, embodied in Eqs. (1) and (4) by using the following relations between the invariants of $\mathbf{B}$ and the principal stretches:

$$\begin{aligned} I_1 &= \lambda_1^2 + \lambda_2^2 + \lambda_3^2 \\ I_2 &= \frac{1}{2}\left[\left(\lambda_1^2 + \lambda_2^2 + \lambda_3^2\right)^2 - \lambda_1^4 - \lambda_2^4 - \lambda_3^4\right] = \lambda_1^2\cdot\lambda_2^2 + \lambda_1^2\cdot\lambda_3^2 + \lambda_2^2\cdot\lambda_3^2 \\ I_3 &= \lambda_1^2\cdot\lambda_2^2\cdot\lambda_3^2 \end{aligned} \tag{5}$$

2.2. Hyperelastic models

A common family among the hyperelastic models is the polynomial models' family. In those models, the strain energy function W is written as a polynomial function of the invariants I_1, I_2, where I_3 is neglected under incompressibility assumption. The general form of the strain energy density function W is:

$$W(\mathbf{B}) = \sum_{i,j=0}^{n} C_{ij}(I_1 - 3)^i(I_2 - 3)^j \tag{6}$$

Where $C_{00} = 0$ and n determines the complexity of the model. Two simple and common models from this family are *Neo-Hookean model* (NH) and *Mooney–Rivlin model* (MR). The strain energy density functions for those models are detailed in the following equations respectively.

$$W^{NH}(\mathbf{B}) = C_{10}(I_1 - 3) = C_{10}(\lambda_1^2 + \lambda_2^2 + \lambda_3^2 - 3) \tag{7}$$

$$\begin{aligned} W^{MR}(\mathbf{B}) &= C_{10}(I_1 - 3) + C_{01}(I_2 - 3) \\ &= C_{10}(\lambda_1^2 + \lambda_2^2 + \lambda_3^2 - 3) + C_{01}(\lambda_1^2\lambda_2^2 + \lambda_2^2\lambda_3^2 + \lambda_3^2\lambda_1^2 - 3) \end{aligned} \tag{8}$$

In addition it is possible to include a *second order* (SO) term in order to get a better fit of the model to the experimental results.

$$\begin{aligned} W^{SO}(\mathbf{B}) &= C_{10}(I_1 - 3) + C_{01}(I_2 - 3) + C_{11}(I_1 - 3)(I_2 - 3) \\ &= C_{10}(\lambda_1^2 + \lambda_2^2 + \lambda_3^2 - 3) + C_{01}(\lambda_1^2\lambda_2^2 + \lambda_2^2\lambda_3^2 + \lambda_3^2\lambda_1^2 - 3) \\ &+ C_{11}(\lambda_1^2 + \lambda_2^2 + \lambda_3^2 - 3)(\lambda_1^2\lambda_2^2 + \lambda_2^2\lambda_3^2 + \lambda_3^2\lambda_1^2 - 3) \end{aligned} \tag{9}$$

Another common model for polymers is *Gent model* (Gent, 1996). In his paper, Gent suggested a modification to Neo-Hookean model for polymers. The model includes a new limiting constant named J_m which is the maximal value of J_1 which defined as the invariant $I_1 - 3$ when the chains of the polymers are fully stretched.

The suggested strain energy function is:

$$W^{Gent}(\mathbf{B}) = -\frac{E}{6} J_m \ln\left[1 - \left(\frac{J_1}{J_m}\right)\right] \tag{10}$$

2.3. Strain hardening model

In his early paper, "Tensile Deformation", Hollomon (1945) suggested the following relation for the plastic deformation with *strain hardening* (SH) of a uniaxial tensile test:

$$\sigma_{zz}^{SH} = K(\varepsilon_{zz})^n \tag{11}$$

Where K and n are material constants and $\sigma_{zz}, \varepsilon_{zz}$ are the axial stress and strain respectively. MC hydrogels display strain thickening behavior due to the non-linearity of the material (McAllister et al., 2015). Strain thickening is represented as an increasing slope in the strain-stress curve for large strains.

2.4. Axial compression in cylindrical coordinates

With the full development for the case of a cylinder under uniaxial compression being detailed in Appendix A, the final expressions are given here.

For the 5 suggested models from Section 2.2, the relations between the axial stress σ_{zz} and the axial stretch Λ, under the assumption of incompressibility are:

$$\sigma_{zz}^{NH}(\Lambda) = 2C_{10}(\Lambda^2 - \Lambda^{-1}) \tag{12}$$

$$\sigma_{zz}^{MR}(\Lambda) = 2C_{10}(\Lambda^2 - \Lambda^{-1}) + 2C_{01}(\Lambda - \Lambda^{-2}) \tag{13}$$

$$\begin{aligned}\sigma_{zz}^{SO}(\Lambda) = {} & 2C_{10}(\Lambda^2 - \Lambda^{-1}) + 2C_{01}(\Lambda - \Lambda^{-2}) \\ & + 6C_{11}(\Lambda^3 - \Lambda^2 - \Lambda + \Lambda^{-1} + \Lambda^{-2} - \Lambda^{-3})\end{aligned} \tag{14}$$

$$\sigma_{zz}^{Gent}(\Lambda) = \frac{E\left(\lambda^2 - \lambda^{-1}\right)}{3\left(1 - \frac{\Lambda^2 - 2\Lambda^{-1} - 3}{J_m}\right)} \tag{15}$$

and the stress–stretch function for the suggested strain hardening model is:

$$\sigma_{zz}^{SH} = K(\Lambda - 1)^n \tag{16}$$

3. Materials and methods

3.1. Gel preparation

MC powder, according to the requested concentrations – 5.6 and 10%Wt – was weighed and added to water. The suspension was mixed and molded into 18 mm diameter vials which were placed in an 80 °C water bath for at least 10 min while stirring. Then, the container was transferred onto an ice bath for at least 60 additional minutes. At this stage, the gels turn from white and opaque to transparent and homogeneous looking liquid solution. Finally, the gel was stored for at least 12 h at 1–4 °C before measurements in glass vials. Right before the experiment, the vials were placed in an 80 °C water bath for 4 min, in order to heat the gel beyond its gelation temperature. Then, the upper part of the vials was carefully shattered, and the gel specimens were extracted. Finally, the upper bubbly part of each specimen was cut and the height of each specimen was measured. This method was developed in order to keep the concentration of the gel during the heating and solidification process. Note that the high fluidity of the gel and the temperature requirements to keep it in the solid state renders tensile testing of e.g. dog bone specimens almost impossible, as opposed to results pertaining to other gels, found in other reports (see e.g. Upadhyay et al. (2020a)). Consequently, the experimental phase will concentrate on uniaxial compression only, while verification will include tensile simulations.

3.2. Experimental setup

Gel compression was performed using INSTRON 4483 testing machine under displacement control. A heating chamber was appended to the compression machine in order to set an ambient temperature of 80 ± 2 °C. The inner temperature in the chamber was continuously monitored using a thermocouple. A water containing vessel was placed in the chamber in order to create a humid environment and reduce water evaporation and desiccation of the gel. Two humidified glass plates were inserted between the loading platens and the specimen. This setup was meant to reduce friction and barreling during the compression. The specimens were compressed at a crosshead speed of $4\left[\frac{mm}{min}\right]$ corresponding to a nominal quasi-static strain rate of $7.0 \cdot 10^{-3}\left[\frac{1}{sec}\right]$. The tests were filmed using high-resolution camera in frame rate of 1 [fps], the deformations were determined using image-processing tools. The experimental setup is presented in Fig. 1.

3.3. Image processing

During the tests, a black background was placed behind the specimen. At 80 °C, the gel is in its solid phase which is white and opaque. After the tests, the contour of the specimen was extracted for each frame during the compression. Then, the axial and radial stretches were calculated by dividing the current height and diameter of the deformed cylinder by the original height and diameter respectively. A photo of the specimen before and after the compression is presented in Fig. 2.

4. Experimental stress–stretch curves

4.1. Incompressibility validation

At the first stage, the relation between the axial and radial stretches was examined. Under incompressibility assumption, a linear relation exists whose slope is $-\frac{1}{2}$ between the logarithms of the radial stretch λ and the axial stretch Λ. The relation between the radial and axial stretches from the experiments is presented in Fig. 3. In some of the curves, there are jumps in the data (marked by arrows). Those disturbances were caused by a leakage of water from the wet upper glass plate during the compression. The drops of water, cause interrupts in the image-processing stage after the test. In order to avoid the effect of those interruptions, the slope was calculated before and after the marked jumps.

One can see that the values of R^2 for all fittings are very close to 1, which indicates a distinct linear relation between $\ln(\lambda)$ and $\ln(\Lambda)$. In addition, the similar slope for all specimens indicates that there is no significant difference between the compressibility of MC gel with different concentrations. From Fig. 3, the average slope $\overline{\nu}$ was calculated and found to be $\overline{\nu} = -0.4155$ what indicates low compressibility of the material. We will assume for the sake of simplicity, and without further testing, that the other types of MC gel at different temperatures exhibit similar incompressibility.

4.2. Compression curves fitting

The 5 suggested models, i.e. Neo-Hookean, Mooney–Rivlin, second-order, Gent and strain hardening, were fitted to Rotbaum et al.'s experimental compression test results (Rotbaum et al., 2017). Three experimental factors were tested, namely MC gel type, MC concentration and test temperature.

Due to the difficulties in performing tension experiments on the gel, the models were fitted according to the compression tests only. care must be exercised in the choice of model in order to avoid instabilities in other loading modes such as tension (Upadhyay et al., 2019). To prevent those instabilities, the models were fitted under constraints, which set limits on the values of the models' constants. The constraints

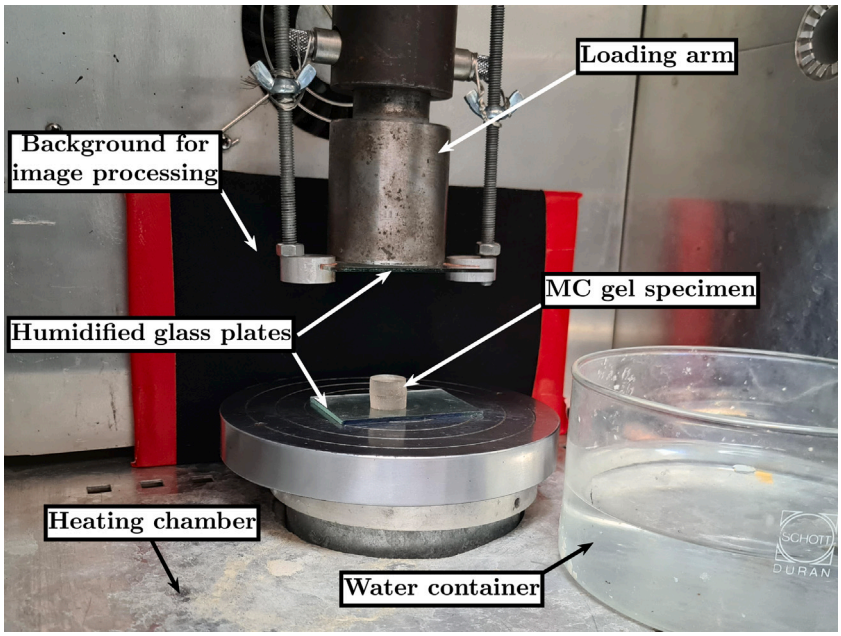

Fig. 1. Experimental setup.

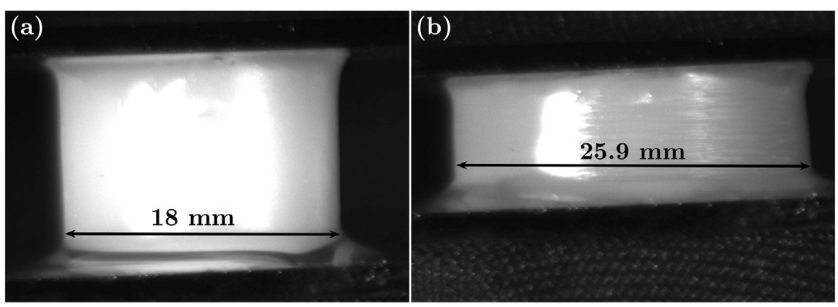

Fig. 2. (a) Undeformed specimen (b) deformed specimen.

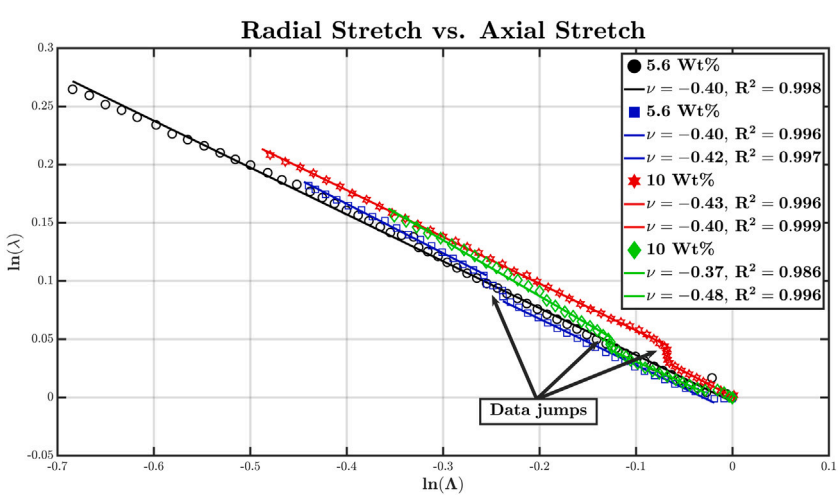

Fig. 3. Relationship between lateral stretch λ and axial stretch Λ.

for the three polynomial models, i.e., Neo-Hookean, Mooney–Rivlin and second order models are developed and detailed in Upadhyay et al. (2019).

All the specimens were compressed at strain rate of $7.5 \cdot 10^{-3} \left[\frac{1}{sec}\right]$. The fitted functions and the raw experimental data are presented in Figs. 4–6. The values of the material's constants which were extracted from the fittings are detailed in Tables 2, 4 and 6. The values of the adjusted r-squared ($\bar{R}^2$), which takes into account the number of free fitting parameters along with the goodness of fit, for the tests and the fitted model are detailed in Tables 3, 5 and 7 in Appendix B.

By comparing the average values of $\bar{R}^2$ for each one of the fitted models, one can see that second order and strain hardening models

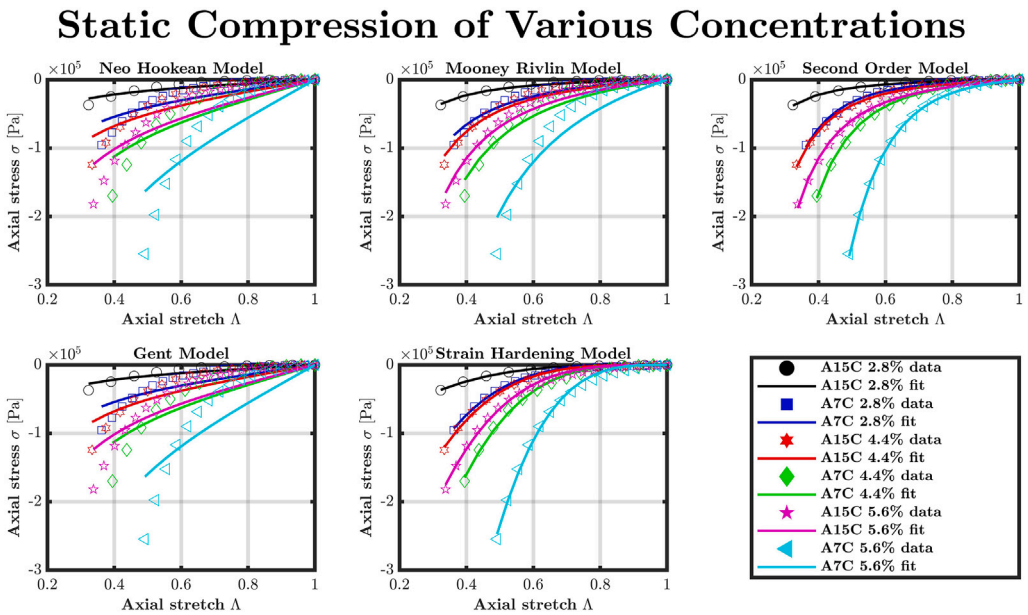

Fig. 4. Quasi-static compression of A7C and A15C MC hydrogels at 80 °C (Rotbaum et al., 2017).

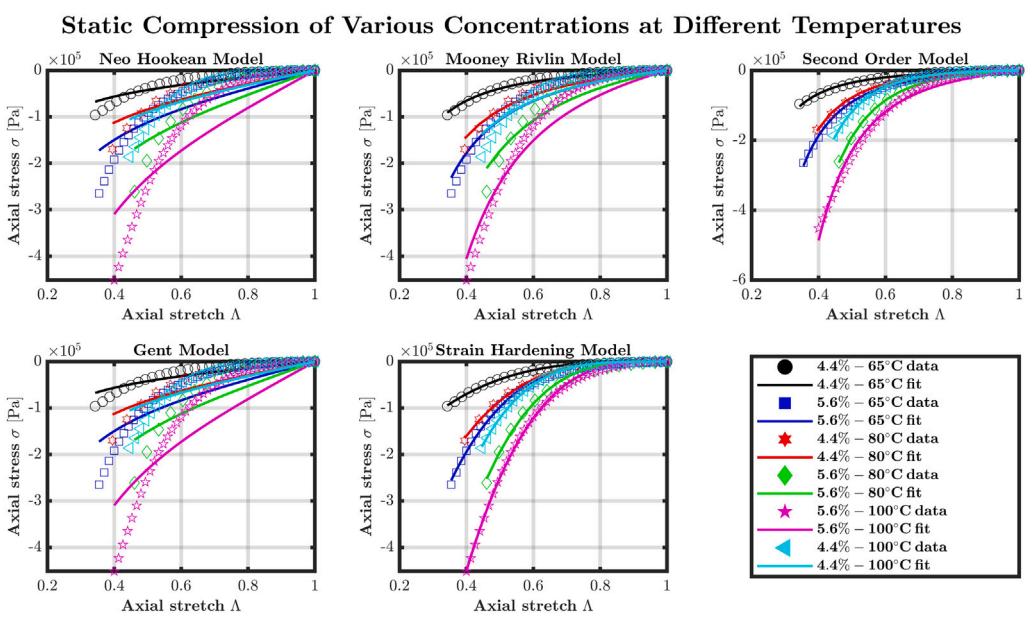

Fig. 5. Quasi-static compression of A7C MC hydrogel with different concentrations at different temperatures (Rotbaum et al., 2017).

yield the highest values of $\bar{R}^2$ (0.996 and 0.995 respectively). Yet, second order model contains an extra model parameter with respect to strain hardening model (3 compared to 2). For Mooney–Rivlin model, the averaged $\bar{R}^2$ value is 0.939 with 2 model constants. Neo-Hookean and Gent model yield the lowest values of $\bar{R}^2$ (less than 0.8) with one and two constants respectively. Note that this comparison between the models refers to the comparison behavior only. The reliability of the models for 3D loading modes will discussed in the next section.

5. Tension prediction

5.1. Predicted stress–stretch curves

In order to assess the reliability of the fitted model, the behavior of the material under tension ($\Lambda > 1$) was predicted, and results are presented in Figs. 7–9.

The predicted tension curves were compared to tension curves of other hydrogels (Upadhyay et al., 2020a,b). Those hydrogels display similar behavior for compression; hence, one can assume similar behavior for tension too. The reported stress–stretch curves display strain hardening for tension (gradient rises with deformation), along with lower strength for tension with respect to compression (lower stress for tension with respect to compression for the same deformation).

Qualitative comparison of the shape of the predicted curves, shows that the only model which displays that kind of mechanical behavior is the second order model. One can see a significant strain hardening in its tension curves. Those exponential shapes of the curves are very similar to the reported curves in Upadhyay et al. (2020a,b).

Neo-Hookean and Gent models, do not display any strain hardening behavior, along with poor values of $\bar{R}^2$ for compression. Mooney–Rivlin model displays a strain-softening behavior, which is not compatible with the reported curves and the phenomenon of strain hardening

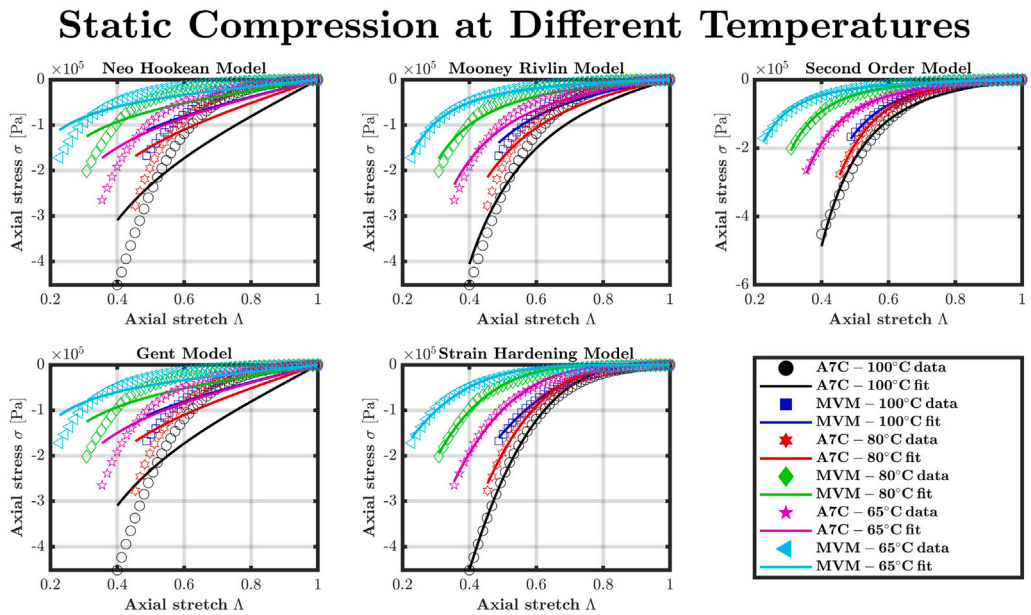

Fig. 6. Quasi-static compression of A7C, A15C and MVM MC hydrogels with concentration of 5.6%Wt at different temperatures (Rotbaum et al., 2017).

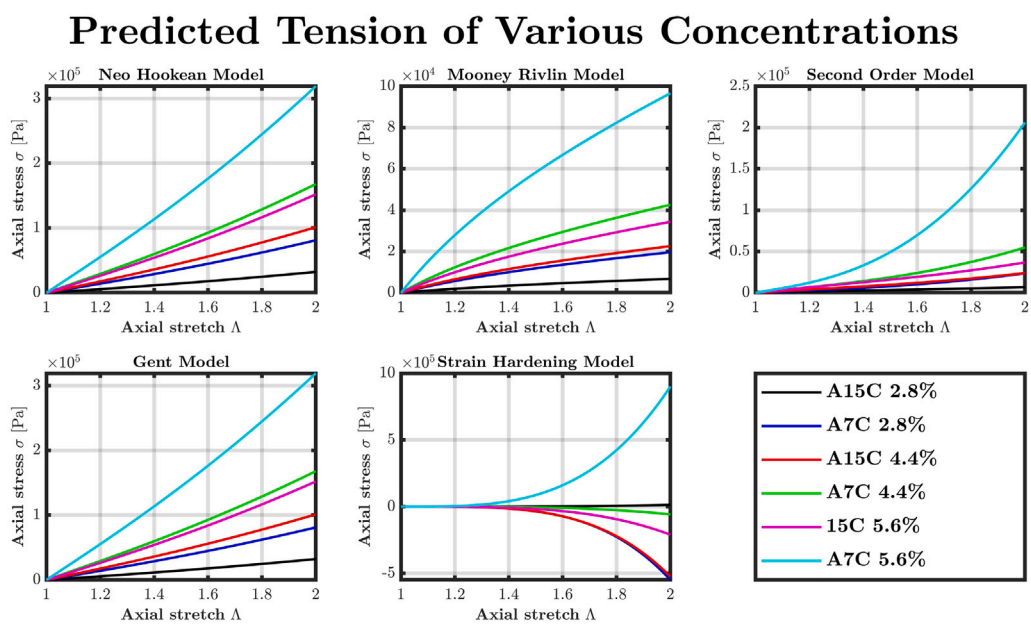

Fig. 7. Quasi-static predicted tension loading of A7C and A15C MC hydrogels at 80 °C.

of cross-linked polymers due to the straitening of the chains. Strain hardening model predicts unstable stress–stretch relationship for part of the curves (negative stresses for tension deformations). Note that this model was not restricted as the hyperelastic models.

6. Discussion

According to the mathematical development in Section 2.4, for an incompressible cylinder under compression, the ratio between the logarithmic axial radial stretch $\ln(\lambda)$ and the logarithmic axial stretch $\ln(\Lambda)$ is -0.5. The experimental results show average ratio of -0.4155 without any dependence of the ratio in the gel's concentration. As a first approximation, we will neglect the slight measured compressibility and assume gel incompressibility. As a result, 4 incompressible hyperelastic models were suggested and fitted to Rotbaum et al.'s results (Rotbaum et al., 2017), in addition to one-dimensional strain hardening model.

Five different models were fitted to the experimental compression results, and the behavior of the material under tension was predicted. The simplest fitted model is Noe-Hookean, which contains only one material constant. However, this model does not describe well the experimental results and its R^2 value is low. Yet, this model predicts reasonable physical behavior for the material, with positive stresses for tension and negative stresses for compression.

The second model that tested is Mooney–Rivlin model. This model was satisfying at describing the mechanical behavior of the material under compression. The model yielded high values of R^2, compared to the number of free material constants. However, the model does not predict a reasonable physical behavior in the tension regime, since it displays strain softening behavior. This model will thus be sufficient for describing the mechanical behavior of the material under compression only but will not describe the material well under other loading modes.

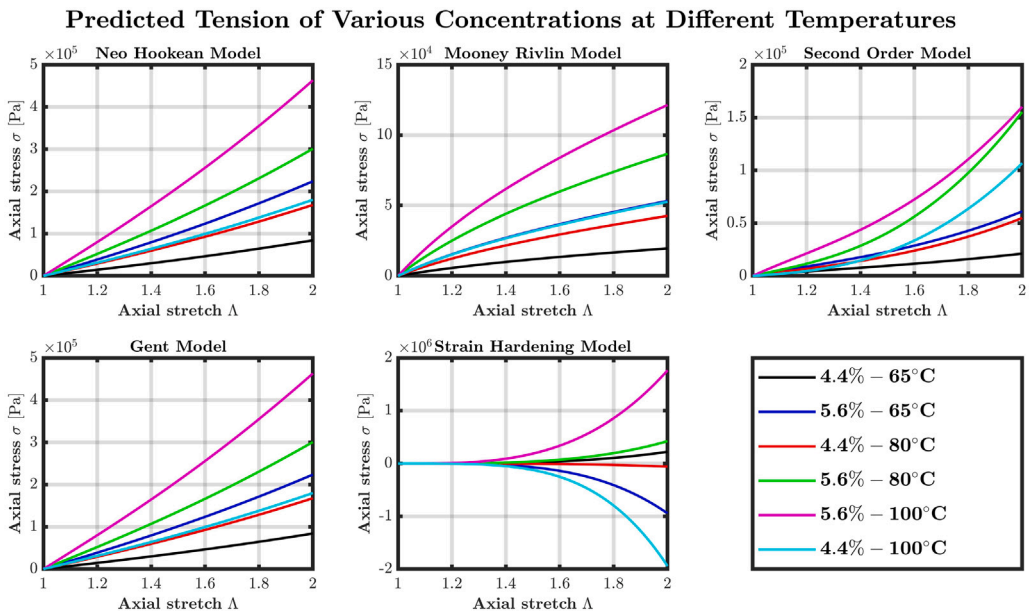

Fig. 8. Quasi-static predicted tension loading of A7C MC hydrogel with different concentrations at different temperatures.

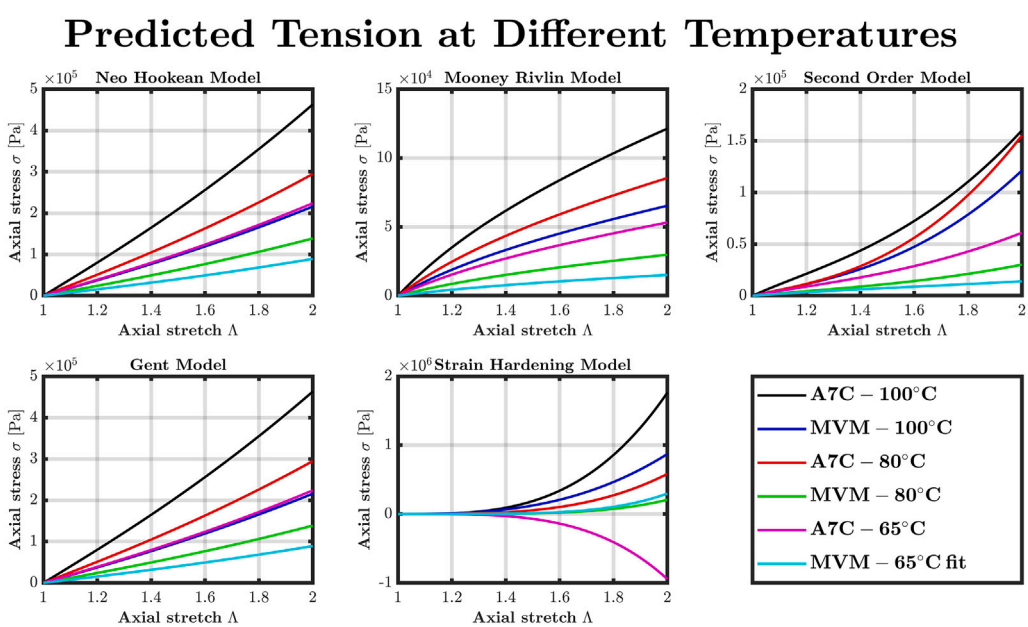

Fig. 9. Quasi-static predicted tension loading of A7C, A15C and MVM MC hydrogels with concentration of 5.6%Wt at different temperatures.

One should notice that the (stability-constrained) values of C_{10} in Mooney–Rivlin and second-order models are almost zero. This means that in order to achieve stability of the model, the first invariant I_1, do not affect the strain energy density function. Yet, the multiplication of the first and second invariants, I_1 and I_2, do affect the strain energy function in the second order model.

The third model (second order) contains 3 material constants. This model yields an almost perfect fit to the compression experimental results, while retaining a convincing apparent physical behavior in the tension regime, when compared to other hydrogels (Upadhyay et al., 2020a,b).

The fourth model (Gent) contains 2 material constants. This model does not describe the experimental results well despite its stability in the tension regime. The model is a modification for Neo-Hookean model for cross-linked polymer, with one more constant. In this case, Gent model does not show any fitting improvement with respect to the Neo-Hookean model.

The last model is the strain hardening model, with only 2 material constants. This model, despite its good fit to the experimental compression results, does not provide reasonable consistent physical behavior for the tension regime. This model's constants were not restricted like the hyperelastic models; hence the tension stability is not achieved.

From the above, it appears that the only model which provides both good fitting, alongside a physical predicted tensile mechanical behavior, is the second order model. Comparing the predicted tension curves to other works (Upadhyay et al., 2020a,b), shows similar qualitative behavior. This comparison justifies the predicted results for untested loading conditions, due to the complexity of the experimental procedure.

The suitability of each model for compression and tension is detailed in Table 1.

Table 1
Suitability of models for compression and tension of MC hydrogels.

	Neo-Hookean	Mooney–Rivlin	Second-order	Gent	Strain hardening
Compression	-	+	+	-	+
Tension	-	-	+	-	-

As a final remark, it is believed that the general methodology and outcomes presented in this work should apply to other kinds of hydrogels beyond the specific MC gels studied here.

7. Conclusions

- Solid MC hydrogels can be reasonably assumed to be incompressible.
- Strain hardening model yielded the best fit for compression with two material constants. However, this model is not suitable for tension dues to its lack of stability.
- The stability constrained value of C_{10} for both Mooney–Rivlin and Second order models is almost zero. The invariant I_1 do not affect the strain energy function.
- The second order model describes best both the tension and the compression of the gel. The predicted tension curves were found to be similar to those reported in other works (Upadhyay et al., 2020a,b).
- Despite the lack of tension experiments, calibration of the model under stability-dictated constraints yields a physical model which is similar to previous reports.

Declaration of competing interest

The authors declare that they have no known competing financial interests or personal relationships that could have appeared to influence the work reported in this paper.

Data availability

The raw/processed data required to reproduce these findings cannot be shared at this time as the data also forms part of an ongoing study.

Acknowledgments

This research was partly supported by grant 2024374 from the Technion PMRI Center for Security Science and Technology, Israel.

The authors wish to acknowledge Dr. Y. Rotbaum for the experimental static compression results and Prof. Y. Eichen and Dr. G. Parvari, Schulich Faculty of Chemistry – Technion, for many enlightening discussions and assistance with the preparation of the gel samples.

Appendix A. Expanded theoretical background

A.1. Hyperelasticity

Consider a deformation in which a point of an isotropic body having coordinates $P_0(X_i)$ is displaced to a new position $P(x_i)$. The deformation gradient tensor which characterizes the mapping is denoted by:

$$F_{ij} = \mathrm{Grad}(\mathbf{x}) \tag{17}$$

Left Cauchy–Green tensor is defined by $\mathbf{F}$:

$$\mathbf{B} = \mathbf{F}\mathbf{F}^{\mathbf{T}} \tag{18}$$

It is convenient to define a set of invariants of $\mathbf{B}$:

$$\begin{aligned} I_1 &= \mathrm{trace}(\mathbf{B}) = B_{kk} \\ I_2 &= \frac{1}{2}\left[(\mathrm{trace}(\mathbf{B})^2 - \mathrm{trace}(\mathbf{B}^2)\right] = \frac{1}{2}(B_{kk} - B_{ik}B_{ki}) \\ I_3 &= \det(\mathbf{B}) = \frac{1}{6}\varepsilon_{stp}\varepsilon_{ijk}B_{si}B_{tj}B_{pk} \end{aligned} \tag{19}$$

where ε_{ijk} represent the Levi-Civita operator.

The resulting stresses in the deformed body are given by:

$$\boldsymbol{\sigma} = \frac{2}{J}\left[\left(\frac{\partial W}{\partial I_1} + I_1\frac{\partial W}{\partial I_2}\right)\mathbf{B} - \frac{\partial W}{\partial I_2}\mathbf{B}^2 + I_3\frac{\partial W}{\partial I_3}\mathbf{1}\right] \tag{20}$$

Where $J = \det(\mathbf{F}) = \sqrt{I_3}$ and $W(\mathbf{B})$ is the strain energy function, that is measured per unit volume of the undeformed body and is a function of these invariants only. Eq. (1) describes the relation between the strain energy density function W and the stress tensor $\boldsymbol{\sigma}$. One can use many different energy functions, depending on the selected hyperelastic model.

Alternatively, one can define the strain energy function as a function of the principal stretches λ_i:

$$W(\mathbf{B}) = W(\lambda_1, \lambda_2, \lambda_3) \tag{21}$$

The principal stretches can be calculated from $\mathbf{B}$:

$$\lambda_i = \sqrt{\zeta_i} \tag{22}$$

where ζ_i is the ith eigenvalue of $\mathbf{B}$. Therefore, we can write $\mathbf{B}$ in its spectral form as:

$$\mathbf{B} = \lambda_1^2 \cdot n^{(1)} \otimes n^{(1)} + \lambda_2^2 \cdot n^{(2)} \otimes n^{(2)} + \lambda_3^2 \cdot n^{(3)} \otimes n^{(3)} \tag{23}$$

where $n^{(i)}$ are the orthonormal eigenvectors of $\mathbf{B}$ that are the principal directions of the deformed body.

By using the spectral decomposition of $\mathbf{B}$, we can find immediately the stress tensor in its spectral form:

$$\sigma_i = \frac{\lambda_i}{\lambda_1\lambda_2\lambda_3}\frac{\partial W}{\partial \lambda_i} \qquad \text{(no sum)} \tag{24}$$

One can switch between those two approaches, corresponding to Eqs. (20) and (24) by using the following relations between the invariants of $\mathbf{B}$ and the principal stretches:

$$\begin{aligned} I_1 &= \lambda_1^2 + \lambda_2^2 + \lambda_3^2 \\ I_2 &= \frac{1}{2}\left[\left(\lambda_1^2 + \lambda_2^2 + \lambda_3^2\right)^2 - \lambda_1^4 - \lambda_2^4 - \lambda_3^4\right] = \lambda_1^2 \cdot \lambda_2^2 + \lambda_1^2 \cdot \lambda_3^2 + \lambda_2^2 \cdot \lambda_3^2 \\ I_3 &= \lambda_1^2 \cdot \lambda_2^2 \cdot \lambda_3^2 \end{aligned} \tag{25}$$

A.2. Hyperelastic models

A common family among the hyperelastic models is the polynomial models' family. In those models, the strain energy function W is written as a polynomial function of the invariants I_1, I_2, where I_3 is neglected due to incompressibility assumption. The general form of the strain energy density function W is:

$$W(\mathbf{B}) = \sum_{i,j=0}^{n} C_{ij}(I_1 - 3)^i(I_2 - 3)^j \tag{26}$$

Where $C_{00} = 0$ and n determines the complexity of the model. Two simple and common models from this family are ***Neo-Hookean model*** and ***Mooney–Rivlin model***. The strain energy density functions for those models are detailed in the following equations respectively.

$$W^{NH}(\mathbf{B}) = C_{10}(I_1 - 3) = C_{10}(\lambda_1^2 + \lambda_2^2 + \lambda_3^2 - 3) \tag{27}$$

$$\begin{aligned} W^{MR}(\mathbf{B}) &= C_{10}(I_1 - 3) + C_{01}(I_2 - 3) \\ &= C_{10}(\lambda_1^2 + \lambda_2^2 + \lambda_3^2 - 3) + C_{01}(\lambda_1^2\lambda_2^2 + \lambda_2^2\lambda_3^2 + \lambda_3^2\lambda_1^2 - 3) \end{aligned} \tag{28}$$

Table 2
Constants values for the suggested models fitted to static compression experimental results of A7C and A15C MC hydrogels at 80 °C.

Constant	Neo-Hookean	Mooney–Rivlin		Second order			Gent		Strain hardening	
	C_{10}	C_{10}	C_{01}	C_{10}	C_{01}	C_{11}	E	J_m	K	n
A15C 2.8%Wt	4604.37	9.39E−07	1922.72	5.20E−07	1473.14	101.85	27626.27	−2683508.01	−141068.00	3.47
A7C 2.8%Wt	11578.19	7.80E−07	5607.08	6.56E−05	2593.92	919.26	69469.16	−1425536.22	−553407.13	3.96
A15C 4.4%Wt	14462.37	7.39E−07	6447.89	2.82E−06	3791.12	674.18	86774.25	−2645096.73	−578120.59	3.86
A7C 4.4%Wt	23973.70	2.17E−05	12168.87	8.86E−07	6214.89	2100.57	143842.30	−1533373.45	−963418.41	3.52
A15C 5.6%Wt	21706.46	6.87E−07	9814.01	2.08E−06	6393.07	908.67	130238.89	−1545393.11	−767909.48	3.59
A7C 5.6%Wt	45564.23	1.71E−06	27588.90	7.90E−06	9647.56	10933.76	273385.42	−3076938.41	−2434475.77	3.38

In addition it is possible to include a **second order** term in order to get a better fit of the model to the experimental results.

$$\begin{aligned} W^{SO}(\mathbf{B}) &= C_{10}(I_1-3)+C_{01}(I_2-3)+C_{11}(I_1-3)(I_2-3) \\ &= C_{10}(\lambda_1^2+\lambda_2^2+\lambda_3^2-3)+C_{01}(\lambda_1^2\lambda_2^2+\lambda_2^2\lambda_3^2+\lambda_3^2\lambda_1^2-3) \\ &+ C_{11}(\lambda_1^2+\lambda_2^2+\lambda_3^2-3)(\lambda_1^2\lambda_2^2+\lambda_2^2\lambda_3^2+\lambda_3^2\lambda_1^2-3) \end{aligned} \tag{29}$$

A.3. Strain hardening model

In his paper, "Tensile Deformation", Hollomon (1945) suggested the following relation for the plastic deformation with strain hardening of uniaxial tensile:

$$\sigma_{zz}^{SH} = K(\varepsilon_{zz})^n \tag{30}$$

Where K and n are material constants and $\sigma_{zz}, \varepsilon_{zz}$ are the axial stress and strain respectively. MC hydrogels display strain thickening behavior due to the non-linearity of the material (McAllister et al., 2015). This strain thickening is represented as an increasing slope in the strain-stress curve for large strains. This phenomenon, may render this strain hardening model useful for describing the mechanical behavior of MC hydrogels.

A.4. Axial compression in cylindrical coordinates

Consider the case of a cylinder under axial compression without any friction between the cylinder ends and the compressing planes. A cylindrical coordinates system $\mathbf{G}_i$ is located in the middle of the undeformed body. A body point which was in the location $X = (R, \Phi, Z)$ is now located in $x = (r, \phi, z)$ in the cylindrical coordinates system $\mathbf{g}_i$ in the deformed body. Under the assumption of axial symmetry, the deformed body remains a cylinder during the deformation and there is no dependence of the displacement on the coordinate Φ. The relation between the coordinates of a deformed body point to its undeformed coordinates is:

$$\begin{aligned} r &= \lambda \cdot R \\ \phi &= \Phi \\ z &= \Lambda \cdot Z \end{aligned} \tag{31}$$

Where Λ is the axial stretch and λ is the radial stretch. This relations means that the axial displacement of a material point is dependent only in its axial distance from the origin and the radial displacement is dependent only on its radial displacement.

The deformation gradient $\mathbf{F}$ in cylindrical coordinates is Volokh (2016):

$$\begin{aligned} \mathbf{F} = &\frac{\partial r}{\partial R}\mathbf{g}_r \otimes \mathbf{G}_R + \frac{1}{R}\frac{\partial r}{\partial \Phi}\mathbf{g}_r \otimes \mathbf{G}_\Phi + \frac{\partial r}{\partial Z}\mathbf{g}_r \otimes \mathbf{G}_Z \\ &+ r\frac{\partial \phi}{\partial R}\mathbf{g}_\phi \otimes \mathbf{G}_R + \frac{r}{R}\frac{\partial \phi}{\partial \Phi}\mathbf{g}_\phi \otimes \mathbf{G}_\Phi + r\frac{\partial \phi}{\partial Z}\mathbf{g}_\phi \otimes \mathbf{G}_Z \\ &+ \frac{\partial z}{\partial R}\mathbf{g}_z \otimes \mathbf{G}_R + \frac{1}{R}\frac{\partial z}{\partial \Phi}\mathbf{g}_z \otimes \mathbf{G}_\Phi + \frac{\partial z}{\partial Z}\mathbf{g}_z \otimes \mathbf{G}_Z \end{aligned} \tag{32}$$

Substituting the relation between the deformed and undeformed coordinates from Eq. (31), and the derivatives of the basis vectors $\mathbf{g}_i$:

$$\mathbf{F} = \lambda\, \mathbf{g}_r \otimes \mathbf{G}_R + \lambda\, \mathbf{g}_\phi \otimes \mathbf{G}_\Phi + \Lambda\, \mathbf{g}_z \otimes \mathbf{G}_Z \tag{33}$$

Left Cauchy–Green tensor $\mathbf{B}$ is:

$$\mathbf{B} = \lambda^2\, \mathbf{g}_r \otimes \mathbf{g}_r + \lambda^2\, \mathbf{g}_\phi \otimes \mathbf{g}_\phi + \Lambda^2\, \mathbf{g}_z \otimes \mathbf{g}_z \tag{34}$$

and the invariants of $\mathbf{B}$ are:

$$\begin{aligned} I_1 &= 2\cdot\lambda^2 + \Lambda^2 \\ I_2 &= \lambda^4 + 2\cdot\lambda^2\Lambda^2 \\ I_3 &= \lambda^4\cdot\Lambda^2 \end{aligned} \tag{35}$$

Since MC hydrogels contain mostly water, incompressibility assumption is reasonable. This assumption will be justified later. Under this assumption, $I_3 = 1$ and therefore the following relation between the stretches is exists:

$$\begin{aligned} I_3 &= \lambda^4\cdot\Lambda^2 = 1 \\ \lambda &= \Lambda^{-\frac{1}{2}} \\ \ln\lambda &= -\frac{1}{2}\cdot\ln\Lambda \end{aligned} \tag{36}$$

and the invariants I_1 and I_2 are now:

$$\begin{aligned} I_1 &= 2\Lambda^{-1} + \Lambda^2 \\ I_2 &= \Lambda^{-2} + 2\Lambda \end{aligned} \tag{37}$$

A.4.1. Hyperelastic models for cylinder compression

For the case of axial compression of a cylinder, after substituting the invariants as a function of the axial stretch λ, the strain energy density functions which were detailed in Appendix A.2 are:

$$W^{NH}(\mathbf{B}) = C_{10}(2\Lambda^{-1} + \Lambda^2 - 3) \tag{38}$$

$$W^{MR}(\mathbf{B}) = C_{10}(2\Lambda^{-1} + \Lambda^2 - 3) + C_{01}(\Lambda^{-2} + 2\Lambda - 3) \tag{39}$$

$$\begin{aligned} W^{SO}(\mathbf{B}) = &C_{10}(2\Lambda^{-1} + \Lambda^2 - 3) + C_{01}(\Lambda^{-2} + 2\Lambda - 3) \\ &+ C_{11}(2\Lambda^{-1} + \Lambda^2 - 3)(\Lambda^{-2} + 2\Lambda - 3) \end{aligned} \tag{40}$$

According to Eq. (24), the axial stress σ_{zz} can be calculated by deriving the strain energy functions with respect to Λ:

$$\sigma_{zz}^{NH}(\Lambda) = 2C_{10}(\Lambda^2 - \Lambda^{-1}) \tag{41}$$

$$\sigma_{zz}^{MR}(\Lambda) = 2C_{10}(\Lambda^2 - \Lambda^{-1}) + 2C_{01}(\Lambda - \Lambda^{-2}) \tag{42}$$

$$\begin{aligned} \sigma_{zz}^{SO}(\Lambda) = &2C_{10}(\Lambda^2 - \Lambda^{-1}) + 2C_{01}(\Lambda - \Lambda^{-2}) \\ &+ 6C_{11}(\Lambda^3 - \Lambda^2 - \Lambda + \Lambda^{-1} + \Lambda^{-2} - \Lambda^{-3}) \end{aligned} \tag{43}$$

A.4.2. Strain hardening model for cylinder compression

In Section A.3, a strain hardening model was suggested. It is possible to switch between the axial strain ε_{zz} and the axial stretch Λ according to the following relation:

$$\varepsilon_{zz} = \Lambda - 1 \tag{44}$$

and the stretch–stress function for the suggested **strain hardening** model is:

$$\sigma_{zz}^{SH} = K(\Lambda - 1)^n \tag{45}$$

Table 3
Adjusted R^2 values of the suggested models fitted to static compression experimental results of A7C and A15C MC hydrogels at 80 °C.

	Neo-Hookean	Mooney–Rivlin	Second-order	Gent	Strain hardening
A15C 2.8%Wt	0.826	0.979	0.990	0.807	0.998
A7C 2.8%Wt	0.751	0.932	0.997	0.739	0.995
A15C 4.4%Wt	0.781	0.958	0.995	0.766	0.995
A7C 4.4%Wt	0.779	0.938	0.997	0.762	0.995
A15C 5.6%Wt	0.800	0.968	0.997	0.790	0.993
A7C 5.6%Wt	0.751	0.884	0.999	0.735	0.996

Table 4
Constants values for the suggested models fitted to static compression experimental results of A7C MC hydrogel with different concentrations at different ambient temperatures.

Constant	Neo-Hookean	Mooney–Rivlin		Second order			Gent		Strain hardening	
	C_{10}	C_{10}	C_{01}	C_{10}	C_{01}	C_{11}	E	J_m	K	n
4.4%Wt - 65 °C	12036.91	1.41E−07	5582.73	5.16E−07	3971.98	458.42	72221.48	−2733640.89	−376720.79	3.30
5.6%Wt - 65 °C	31983.73	1.16E−07	15198.84	8.87E−08	8314.35	2024.78	191902.47	−3116884.49	−1322494.96	3.75
4.4%Wt - 80 °C	23973.70	2.17E−05	12168.87	8.86E−07	6214.89	2100.57	143842.30	−1533373.45	−963418.41	3.52
5.6%Wt - 80 °C	43006.67	2.99E−07	24759.75	2.61E−05	9709.63	7697.60	258040.08	−3088987.69	−2104626.36	3.44
5.6%Wt - 100 °C	666154.68	1.89E−07	34679.45	6.27E−05	19822.39	5763.79	396928.13	−6227218.99	−2348771.13	3.23
4.4%Wt - 100 °C	25725.31	2.23E−05	15018.54	4.36E−06	3235.25	6054.56	154351.96	−700037.86	−1943349.97	4.00

Table 5
Adjusted R^2 values of the suggested models fitted to static compression experimental results of A7C MC hydrogel with different concentrations at different ambient temperatures.

	Neo-Hookean	Mooney–Rivlin	Second-order	Gent	Strain hardening
4.4%Wt - 65 °C	0.812	0.974	0.993	0.812	0.997
5.6%Wt - 65 °C	0.770	0.953	0.997	0.770	0.994
4.4%Wt - 80 °C	0.779	0.938	0.997	0.762	0.995
5.6%Wt - 80 °C	0.758	0.900	0.999	0.740	0.994
5.6%Wt - 100 °C	0.786	0.947	0.991	0.785	0.999
4.4%Wt - 100 °C	0.694	0.866	0.999	0.693	0.998

Table 6
Constants values for the suggested models fitted to static compression experimental results of A7C and A15C MC hydrogels with concentration of 5.6%Wt at different ambient temperatures.

Constant	Neo-Hookean	Mooney–Rivlin		Second order			Gent		Strain hardening	
	C_{10}	C_{10}	C_{01}	C_{10}	C_{01}	C_{11}	E	J_m	K	n
A7C - 100 °C	66154.68	1.89E−07	34679.45	6.27E−05	19822.39	5763.79	396928.13	−6227218.99	−2348771.13	3.23
MVM - 100 °C	30846.91	2.56E−05	18676.87	1.16E−06	9981.80	5486.88	185081.49	−3116603.07	−1050399.40	2.81
A7C - 80 °C	42112.84	2.16E−07	24424.61	9.56E−05	9717.86	7693.19	252677.07	−3092436.46	−2056604.82	3.41
MVM - 80 °C	19820.93	9.01E−08	8515.17	3.80E−05	4168.74	984.81	118925.71	−1552207.50	−1047639.96	4.56
A7C - 65 °C	31983.73	1.16E−07	15198.84	8.87E−08	8314.35	2024.78	191902.47	−3116884.49	−1322494.96	3.75
MVM - 65 °C	12746.64	5.98E−08	4321.06	1.82E−07	3392.36	135.11	76479.84	−5268749.95	−536147.83	4.69

Table 7
Adjusted R^2 values of the suggested models fitted to static compression experimental results of A7C and A15C MC hydrogels with concentration of 5.6%Wt at different ambient temperatures.

	Neo-Hookean	Mooney–Rivlin	Second-order	Gent	Strain hardening
A7C - 100 °C	0.786	0.947	0.991	0.785	0.999
MVM - 100 °C	0.804	0.937	0.998	0.803	0.996
A7C - 80 °C	0.752	0.910	0.999	0.751	0.994
MVM - 80 °C	0.740	0.948	0.997	0.740	0.992
A7C - 65 °C	0.770	0.953	0.997	0.770	0.994
MVM - 65 °C	0.796	0.989	0.997	0.796	0.989

Appendix B. Experimental results tables

See Tables 2–7.

References

Alley, M.D., Schimizze, B.R., Son, S.F., 2011. Experimental modeling of explosive blast-related traumatic brain injuries. NeuroImage 54 (5), S45–S54. http://dx.doi.org/10.1016/j.neuroimage.2010.05.030.

Altomare, L., Cochis, A., Carletta, A., Rimondini, L., Farè, S., 2016. Thermo-responsive methylcellulose hydrogels as temporary substrate for cell sheet biofabrication. J. Mater. Sci.: Mater. Med. 27 (5), 1–13. http://dx.doi.org/10.1007/s10856-016-5703-8.

Biswas, P., Mamatha, S., Naskar, S., Rao, Y.S., Johnson, R., Padmanabham, G., 2018. 3D extrusion printing of magnesium aluminate spinel ceramic parts using thermally induced gelation of methyl cellulose. J. Alloys Compd. 770 (8), 419–423. http://dx.doi.org/10.1016/j.jallcom.2018.08.152.

Bonetti, L., De Nardo, L., Farè, S., 2020. Thermo-responsive methylcellulose hydrogels: From design to applications as smart biomaterials. Tissue Eng. B: Rev. 00 (12), 1–23. http://dx.doi.org/10.1089/ten.teb.2020.0202.

ClinCalc LLC, 2021. Methylcellulose - drug usage statistics, United States, 2008–2018, ClinCalc DrugStats database. URL https://clincalc.com/DrugStats/Drugs/Methylcellulose4000MpaS.

Contessi Negrini, N., Bonetti, L., Contili, L., Farè, S., 2018. 3D printing of methylcellulose-based hydrogels. Bioprinting 10 (5), http://dx.doi.org/10.1016/j.bprint.2018.e00024.

Gent, A., 1996. A new constitutive relation for rubber. Rubber Chem. Technol. 69 (9), 59–61. http://dx.doi.org/10.5254/1.3538357.

Guetta, O., Varfman, B.H., Rittel, D., 2020. Shock attenuation characteristics of methylcellulose hydrogels: Phenomenological modeling. J. Mech. Phys. Solids 146 (10), 104220. http://dx.doi.org/10.1016/j.jmps.2020.104220.

Hollomon, J.H., 1945. Tensile deformation. Aime Trans. 12 (2), 1–22,.

Kim, M.H., Kim, B.S., Park, H., Lee, J., Park, W.H., 2018. Injectable methylcellulose hydrogel containing calcium phosphate nanoparticles for bone regeneration. Int. J. Biol. Macromol. 109 (4), 57–64. http://dx.doi.org/10.1016/j.ijbiomac.2017.12.068.

Klemm, D., Heublein, B., Fink, H.P., Bohn, A., 2005. Cellulose: Fascinating biopolymer and sustainable raw material. Angew. Chem. Int. Edn 44 (5), 3358–3393. http://dx.doi.org/10.1002/anie.200460587.

Law, N., Doney, B., Glover, H., Qin, Y., Aman, Z.M., Sercombe, T.B., Liew, L.J., Dilley, R.J., Doyle, B.J., 2018. Characterisation of hyaluronic acid methylcellulose hydrogels for 3D bioprinting. J. Mech. Behav. Biomed. Mater. 77 (1), 389–399. http://dx.doi.org/10.1016/j.jmbbm.2017.09.031.

McAllister, J.W., Lott, J.R., Schmidt, P.W., Sammler, R.L., Bates, F.S., Lodge, T.P., 2015. Linear and nonlinear rheological behavior of fibrillar methylcellulose hydrogels. ACS Macro Lett. 4 (4), 538–542. http://dx.doi.org/10.1021/acsmacrolett.5b00150.

Nasatto, P., Pignon, F., Silveira, J., Duarte, M., Noseda, M., Rinaudo, M., 2015. Methylcellulose, a cellulose derivative with original physical properties and extended applications. Polymers 7 (4), 777–803. http://dx.doi.org/10.3390/polym7050777.

Noemi, Z., 2011. Edible coatings to improve food quality and safety. In: Food Engineering Interfaces. Springer, pp. 631–660. http://dx.doi.org/10.1007/978-1-4419-7475-4_27.

Parvari, G., Rotbaum, Y., Eichen, Y., Rittel, D., 2018. Impact-induced gelation in aqueous methylcellulose solutions. Chem. Commun. 54 (9), 12578–12581. http://dx.doi.org/10.1039/c8cc06378h.

Polamaplly, P., Cheng, Y., Shi, X., Manikandan, K., Kremer, G.E., Qin, H., 2019. 3D printing and characterization of hydroxypropyl methylcellulose and methylcellulose for biodegradable support structures. Proc. Manuf. 34, 552–559. http://dx.doi.org/10.1016/j.promfg.2019.06.219.

Qiu, X., Hu, S., 2013. "Smart" materials based on cellulose: A review of the preparations, properties, and applications. Materials 6 (2), 738–781. http://dx.doi.org/10.3390/ma6030738.

Rotbaum, Y., Parvari, G., Eichen, Y., Rittel, D., 2017. Static and dynamic large strain properties of methyl cellulose hydrogels. Macromolecules 50 (12), 4817–4826. http://dx.doi.org/10.1021/acs.macromol.7b00270.

Rotbaum, Y., Parvari, G., Eichen, Y., Rittel, D., 2019. Linear and nonlinear shock attenuation of aqueous methylcellulose solutions. Int. J. Impact Eng. 136 (9), 103392. http://dx.doi.org/10.1016/j.ijimpeng.2019.103392.

Schupper, N., Shnerb, N.M., 2005. Inverse melting and inverse freezing: A spin model. Phys. Rev. E - Stat. Nonlinear Soft Matter Phys. 72 (10), 1–16. http://dx.doi.org/10.1103/PhysRevE.72.046107.

Senol, K., Parvari, G., Rotbaum, Y., Eichen, Y., Rittel, D., Shukla, A., 2020. Mitigation of shock loading on structures using aqueous methylcellulose solution. Int. J. Impact Eng. 140 (2), 734–743. http://dx.doi.org/10.1016/j.ijimpeng.2020.103547.

Stalling, S.S., Akintoye, S.O., Nicoll, S.B., 2009. Development of photocrosslinked methylcellulose hydrogels for soft tissue reconstruction. Acta Biomater. 5 (7), 1911–1918. http://dx.doi.org/10.1016/j.actbio.2009.02.020.

Truesdell, C., Noll, W., Truesdell, C., Noll, W., 2004. The Non-Linear Field Theories of Mechanics. Springer, pp. 1–579. http://dx.doi.org/10.1007/978-3-662-10388-3_1.

Upadhyay, K., Subhash, G., Spearot, D., 2019. Thermodynamics-based stability criteria for constitutive equations of isotropic hyperelastic solids. J. Mech. Phys. Solids 124 (9), 115–142. http://dx.doi.org/10.1016/j.jmps.2018.09.038.

Upadhyay, K., Subhash, G., Spearot, D., 2020a. Hyperelastic constitutive modeling of hydrogels based on primary deformation modes and validation under 3D stress states. Internat. J. Engrg. Sci. 154, 103314. http://dx.doi.org/10.1016/j.ijengsci.2020.103314.

Upadhyay, K., Subhash, G., Spearot, D., 2020b. Visco-hyperelastic constitutive modeling of strain rate sensitive soft materials. J. Mech. Phys. Solids 135, http://dx.doi.org/10.1016/j.jmps.2019.103777.

Volokh, K., 2016. Mechanics of Soft Materials. Springer, pp. 1–155. http://dx.doi.org/10.1007/978-981-10-1599-1.